A Letters Journal Exploring the Frontiers of Physics

October 2019

EPL, **128** (2019) 14003
doi: 10.1209/0295-5075/128/14003

www.epljournal.org

Mitigation of oscillatory instability in turbulent reactive flows: A novel approach using complex networks

Abin Krishnan[1], R. Manikandan[1], P. R. Midhun[1], K. V. Reeja[1], V. R. Unni[2], R. I. Sujith[1], Norbert Marwan[3] and Jürgen Kurths[3,4,5]

[1] *Indian Institute of Technology Madras - Chennai 600036, India*
[2] *University of California San Diego - San Diego, CA 92093, USA*
[3] *Potsdam Institute for Climate Impact Research - Potsdam 14412, Germany*
[4] *Humboldt University Berlin - Newtonstr. 15, 12489 Berlin, Germany*
[5] *Institute for Complex Systems and Mathematical Biology, University of Aberdeen - Aberdeen AB 24 UE, UK*

received 19 August 2019; accepted in final form 7 October 2019
published online 27 November 2019

PACS 43.28.Kt – Aerothermoacoustics and combustion acoustics
PACS 89.75.Hc – Networks and genealogical trees
PACS 47.27.Rc – Turbulence control

Abstract – We present a novel and an efficient way to mitigate oscillatory instability in turbulent reactive flows. First, we construct weighted spatial correlation networks from the velocity field obtained from high-speed particle image velocimetry. Using network measures, we identify the optimal location for implementing passive control strategies. By injecting micro-jets at this optimal location, we are able to reduce the amplitude of the pressure oscillations to a value comparable to what is observed during the state of stable operation. This approach opens up new avenues to control oscillatory instabilities in turbulent flows.

Introduction. – Half a century ago, Neil Armstrong would not have landed on the Moon on July 20, 1969 if the Apollo engineers did not come up with a solution to the problem of thermoacoustic instability. This is reflected in the words of Saverio "Sonny" F. Morea, the F1 engine project director[1]: "Combustion instability was one of the biggest challenges of the Apollo programme. If we didn't come up with a solution, we weren't going to the Moon". Thermoacoustic instability, also known as combustion instability, refers to the phenomenon of spontaneous excitation of large-amplitude periodic acoustic pressure oscillations in confinements such as boilers, rocket motors and gas turbines engines [1]. Thermoacoustic instability occurs due to the positive feedback between the unsteady heat release rate fluctuations from the flame and the acoustic pressure fluctuations inside the confinement [2]. As the acoustic driving overcomes the damping, the amplitude of the pressure fluctuation increases and saturates at large-amplitude limit cycle oscillations. These large-amplitude limit cycle oscillations often lead to a sudden failure of engine components and associated electronics, increased heat transfer that overwhelms the thermal protection system and in some cases even mission failures [3].

Control of thermoacoustic instability has attracted the attention of various researchers. There are mainly two approaches to control this oscillatory instability —active and passive. i) Active control measures include the use of actuators such as loudspeakers and oscillatory air/fuel injection [4]. Even though active control approaches are successful over a wide range of frequencies, the practical implementation of these methods adds complexity to the system as they involve the use of electro-mechanical components. ii) In contrast, passive control measures involve simple geometrical modifications, such as the use of acoustic liners, baffles, Helmholtz resonators, modification of the fuel injector geometry/location or the use of micro-jet injection [5]. Since passive control approaches are simple and robust, they have found applications in various practical systems. However, there is one major drawback associated with these passive control approaches. These are based on lots of trials, which are mostly a hit-or-miss approach. The engineers of the Apollo programme had to perform around 3200 full-scale tests, probably the most

[1]The quote is taken from an image showing the F1 engine injector baffle, which is displayed at the U.S. Space and Rocket Center, Huntsville, AL (http://heroicrelics.org/ussrc/engines-f-1-injector-baffle/dsc79618.jpg.html).

intensive and expensive programme ever devoted to solving the problem of thermoacoustic instability, to arrive at a stable liquid rocket motor configuration for the lunar mission [6]. Thus, the control of thermoacoustic instability in practical systems is still a very challenging problem.

We could drastically improve the effectiveness of passive control measures if we are able to determine the optimal location for their implementation. One such optimal location is the region in the flow field that controls the spatiotemporal dynamics during thermoacoustic instability. We refer to this optimal location as the "critical region". Then, the question arises:"how to identify it?"

In this letter, we show that a complex network approach provides an efficient way for the identification of the critical region. Complex network theory has emerged as one of the most efficient tools for the analysis of diverse systems [7–10]. In network theory, the nodes of the network represent the system components and the links represent the interactions between them. High values of network measures such as degree, closeness centrality, betweenness centrality, to name a few, help to identify the critical nodes of the network [11,12]. These network measures have been used to uncover spatial patterns in brain networks [13–15], climate networks [16–19] and fluid flows [20–22]. Also, network measures have been used to suggest the optimal location to control forest fires [23], the spread of mobile malware [24] and turbulent flows [25]. Using spatial correlation network analysis, we have recently characterized the spatial dynamics of a turbulent combustor during stable operation, thermoacoustic instability and the transition regime from stable operation to thermoacoustic instability known as intermittency [26]. We then postulated that network analysis could be used to optimize the control of oscillatory instability [27].

In the current study, we perform experiments in a laboratory-scale bluff body stabilized turbulent combustor with a backward facing step. Here, we construct weighted spatial correlation networks from the velocity field obtained from high-speed particle image velocimetry (PIV), a laser-based optical diagnostic technique [28]. We uncover that the critical region identified by network analysis is indeed the optimal location to implement passive control measures, thus proving that complex networks provide a novel and efficient way to control oscillatory instabilities.

Experimental setup. – The combustion chamber is 1100 mm long and has a cross-section of $90 \times 90\,\mathrm{mm}^2$. A circular disk of 47 mm diameter is used to stabilize the flame (refer to appendix A of the supplemental material `Supplementarymaterial.pdf` (SM) for more details). We fix the fuel (liquefied petroleum gas) flow rate ($\dot{m}_f = 30 \pm 0.44$ SLPM) and vary the air flow rate ($480 \pm 7.84 \leq \dot{m}_a \leq 780 \pm 10.24$ SLPM), thus decreasing the equivalence ratio ($\phi = (\frac{\dot{m}_f}{\dot{m}_a})_{actual}/(\frac{\dot{m}_f}{\dot{m}_a})_{stochiometry}$) from 0.97 to 0.57; with a maximum uncertainty of ± 0.02 in ϕ. Accordingly, the Reynolds number (Re) varies from 1.93×10^4 to 3.13×10^4 with a maximum uncertainty of ± 400 (1.28%).

We measure the acoustic pressure fluctuations using a piezoelectric transducer (with an uncertainty of ± 0.15 Pa), located 20 mm downstream of the backward facing step. A pair of quartz windows ($400 \times 90 \times 10\,\mathrm{mm}^3$) is provided on the side walls of the combustion chamber to facilitate optical diagnostic techniques such as high-speed chemiluminescence and high-speed PIV. High-speed chemiluminescence is used to capture the local heat release rate fluctuations of the flame [29] and high-speed PIV [28] is used to obtain the instantaneous velocity field in the combustor (see appendix B of the SM for more details).

Identification of the critical region. – To identify the critical region, we first construct weighted spatial correlation networks from the velocity field obtained from high-speed PIV. Weighted correlation network analysis has been used extensively in biology [30–32] and finance [33,34]. In the analysis of PIV, we divide the turbulent reactive flow field into a rectangular grid. We regard the cells of this rectangular grid as the nodes of the network. The connectivity between two nodes i and j is based on the Pearson's correlation coefficient ($-1 \leq R_{ij} \leq 1$) between the time series of total velocity ($V(t) = \sqrt{V_x(t)^2 + V_y(t)^2}$) at the two nodes, which is calculated as

$$R_{ij} = \frac{\langle V(i,t)V(j,t)\rangle - \langle V(i,t)\rangle\langle V(j,t)\rangle}{\sigma(V(i))\sigma(V(j))}, \qquad (1)$$

where $\sigma^2(V(i)) = \langle V(i,t)^2\rangle - \langle V(i,t)\rangle^2$ and $\langle\cdot\rangle$ represents the temporal average computed over 3500 samples corresponding to a duration of 1.5 s. Two nodes are connected if $R_{ij} \geq 0.5$. To capture the strength of the interaction between the two locations, we consider R_{ij} ($\geq$0.5) as the weight (w_{ij}) of the link; the higher the value of R_{ij}, the stronger the interaction between the two spatial locations in the turbulent reactive flow field. In this manner, we construct weighted spatial correlation networks for the three dynamical states of the combustor operation namely, the stable state, intermittency and thermoacoustic instability.

We use three network measures to characterize the importance of a node in the network. First, the *strength of a node* [9], which is given by

$$s_i = \sum_{j=1}^{N} w_{ij}, \qquad (2)$$

where N is the total number of nodes and w_{ij} is the weight of the link between the nodes i and j. The number of nodes (N) during the states of stable operation, intermittency and thermoacoustic instability are 2835, 2835 and 2728, respectively (refer to appendix B of the SM for further details). A high value of s_i implies that the time series of velocity at a given location is highly correlated with that of different locations in the flow field. Second, we use the *weighted local clustering coefficient* [35] to characterize the strength of interaction among the neighbours of a node,

which is given by

$$\tilde{C}_i = \frac{\sum_{j,k} w_{ij} w_{jk} w_{ik}}{\max(w) \sum_{j,k} w_{ij} w_{ki}}, \tag{3}$$

where j, k are the neighbours of the node i; $\max(w)$ is the maximum weight in the network. A node with a high s_i and a high $\tilde{C}_i$ implies that the velocity variations at the given node and among its neighbours are strongly correlated. Hence, we can say that the neighbourhood of the given node represents a spatially coherent velocity field. Third, we use the *weighted closeness centrality* [36] to identify the nodes in the network, which is closest to all other nodes and hence can reach them quickly. It is given by

$$\tilde{c}_i = \sum_{j=1, j\neq i}^{N} 2^{-d_w(i,j)}, \tag{4}$$

where $d_w(i,j)$ is the least costly path between the nodes i and j. Here, we consider a path as costly, when it consumes more effort for a piece of information to travel from a node i to another node j. Perturbations tend to reach all other parts of the flow field quickly via highly correlated paths. Hence, we consider the cost of a link as the inverse of R_{ij}. The higher the values of R_{ij} for the paths from a node to all other nodes, the lower the costs and hence the quicker the disturbances reach all other nodes in the network.

The spatial distributions of the weighted network properties, namely s (a), $\tilde{C}$ (b) and $\tilde{c}$ (c) during stable operation, intermittency and thermoacoustic instability are illustrated in fig. 1. The grey rectangular region in the bottom right corner of the subplots is the bluff body. The color bars gives the range of the respective network properties. We observe very high values of s only during thermoacoustic instability, near the backward facing step, above the bluff body shaft. The node strength is two orders of magnitude higher than that during the states of stable operation and intermittency. This region also has very high $\tilde{C}$. Hence, we can say that the velocity variations in the region are highly correlated among themselves as we connect only those nodes where the correlation between the velocity variations is at least 50%. In other words, the region near the backward facing step, above the bluff body shaft, is spatially coherent regarding the velocity variation. High values of these network measures are due to the periodic coherent motion of the flow at the combustor inlet, which eventually self-organizes to form periodic large-scale coherent structures during thermoacoustic instability [37]. Also, we see that the above-mentioned region has high values of $\tilde{c}$. Hence, we can infer that any perturbation given to the region above the bluff body shaft will reach all other parts of the flow field quickly. From the high values of the spatial distribution of these network measures, we find that the region downstream of the backward facing step, on top of the bluff body shaft, emerges as the most critical region at the onset of thermoacoustic instability. We can thus hypothesize that any passive control strategies could be directed at this critical region to mitigate thermoacoustic oscillations. The critical region does not change much when the threshold correlation coefficient (R_t) is varied from 0.3 to 0.7 (refer to appendix C of the SM).

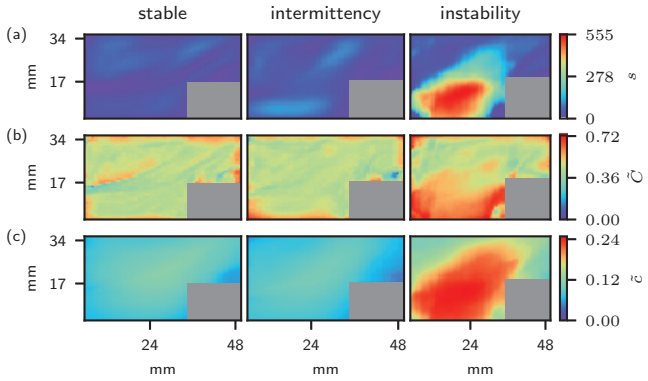

Fig. 1: The spatial distribution of the three weighted network properties s (a), $\tilde{C}$ (b) and $\tilde{c}$ (c) during stable operation, intermittency and thermoacoustic instability, respectively. The grey rectangular region in the bottom right corner of the subplots is the mask used to cover the bluff body in the analysis of PIV (it is to mask the laser light reflections from the bluff body). The region above the bluff body shaft downstream of the backward facing step emerges as the critical region at the onset of thermoacoustic instability.

Smart passive control. – In the present study, we use air micro-jet injection as a passive control measure to mitigate thermoacoustic oscillations. To this end, we divide the flow field into three regions namely, region A (upstream of the bluff body), region B (around the bluff body) and region C (downstream of bluff body). Figure 2 shows the top half cross-section of the combustor with the three regions A, B and C along with the micro-jet injection ports. Region A has a pair of ports at the backward facing step, inclined at an angle (60°) such that the micro-jets target the critical region identified in fig. 1. In addition, we also have two pairs of ports, 10 mm apart, in the top and bottom walls of the combustor in region A. Region B has a pair of ports at the front-end tip of the bluff body, 45 mm downstream of the backward facing step. Finally, region C has a pair of ports 20 mm downstream of the bluff body.

We inject the micro-jet in steps of 5 SLPM to a maximum flow rate of 25 ± 1.2 SLPM through each of the ports. Figure 3 shows the variation of the root-mean-square value of the acoustic pressure fluctuations (p'_{rms}) for the different micro-jet injection locations with respect to the total momentum flux ratio, $(v_j/v_a)^2$. Here, v_j refers to the micro-jet velocity and v_a refers to the velocity of the air at the combustor inlet. The situation corresponding to $(v_j/v_a)^2 = 0$ is the baseline case where the turbulent thermoacoustic system exhibits limit cycle oscillations. For

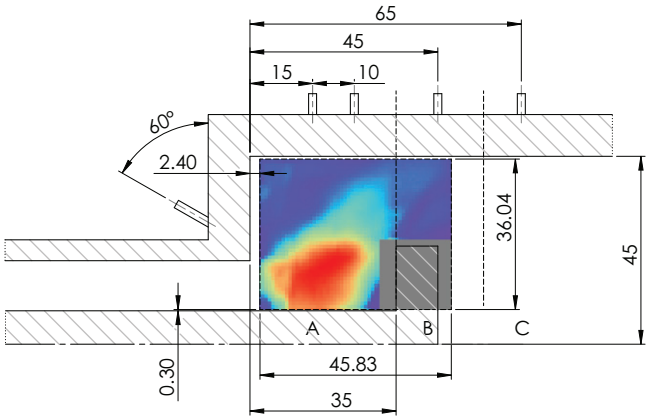

Fig. 2: The cross-section of the top half of the combustion chamber showing the micro-jet injection locations with respect to the spatial distribution of s during thermoacoustic instability. The flow field is divided into three regions, namely A, B and C. In region A, the micro-jets are injected from two locations targeting the critical region identified in fig. 1. Each of the ports has a diameter of 5 mm.

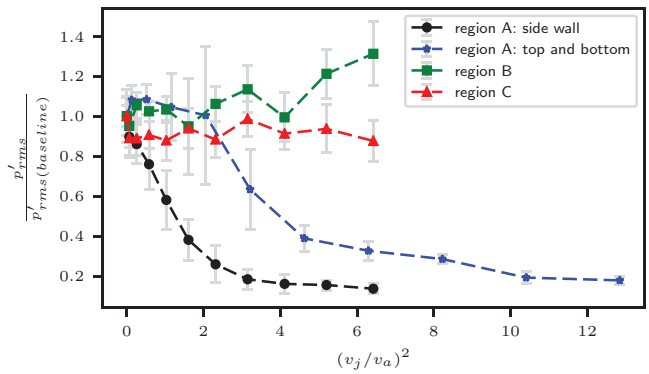

Fig. 3: The variation of p'_{rms} of thermoacoustic oscillations due to injection of micro-jets in regions A, B and C with respect to $(v_j/v_a)^2$. The situation corresponding to $(v_j/v_a)^2 = 0$ is the baseline case where the turbulent thermoacoustic system exhibits limit cycle oscillations. For region A, we get a suppression of around 85% for both the cases of micro-jet injections. The error bars represent the standard deviation. The maximum uncertainty in the calculation of $(v_j/v_a)^2$ is ±7%.

each of the micro-jet injection cases, the p'_{rms} is normalized by the corresponding one during thermoacoustic instability ($p'_{rms(baseline)}$; at $(v_j/v_a)^2 = 0$). As we increase $(v_j/v_a)^2$, we obtain a suppression of about 86% (17 dB) and 83% (15 dB) in p'_{rms} for the side wall and top and bottom wall injections in region A, respectively. After suppression, we get $p'_{rms} \approx 200$ Pa, which is close to the value observed during the stable state of combustor operation ($p'_{rms} \approx 100$ Pa).

As we obtain suppression of thermoacoustic oscillations with micro-jet injection from both the locations in region A, we can conclude that the orientation of the micro-jet injection targeting the critical region does not matter.

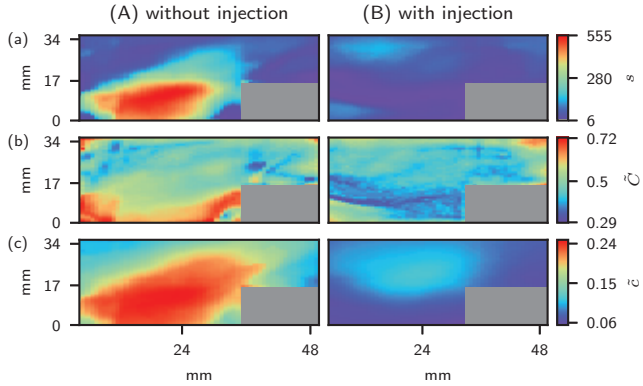

Fig. 4: The variation of s, $\tilde{C}$ and $\tilde{c}$ during (A) thermoacoustic instability and (B) during suppression of thermoacoustic instability with micro-jet injection. Here, the micro-jet is injected from the backward facing step of the combustor targeting the critical region ($(v_j/v_a)^2 = 6.41$). We observe that the region on top of the bluff body shaft no longer remains as the critical region with the suppression of thermoacoustic oscillations.

However, the optimal $(v_j/v_a)^2$ for which we get the suppression differs for both cases of injection. This is because the location of the side wall injection is closer to the critical region than the location of top and bottom wall injection (fig. 2). A reduction of 100% in p'_{rms} is not possible as the inlet flow is turbulent and even the p'_{rms} during the stable operation is approximately 100 Pa. Further, we do not obtain any reduction in p'_{rms} for micro-jet injection in ports located in regions B and C, respectively. Hence, from fig. 3, we can ascertain that the critical region identified using weighted network analysis is indeed the optimal location to implement the passive control strategy. With micro-jet injection at the optimal location, we are able to shift the turbulent combustor with oscillatory instability back to the state of stable operation. The optimal momentum flux ratio, which suppresses thermoacoustic oscillations, however, may differ for different combustor designs.

Next, we again perform high-speed PIV when thermoacoustic oscillations are suppressed with micro-jet injection. We then perform the weighted spatial correlation network analysis to examine the effect of micro-jet injection on the critical region identified in fig. 1. We observe that the region above the bluff body shaft, which was "critical" during thermoacoustic instability, is no more "critical" (fig. 4). We hypothesize that the micro-jets would be disrupting the periodic coherent motion of the flow field during thermoacoustic instability, leading to the loss of correlation between the time series of velocity at different locations in the critical region. This results in very low values of the network measures, when thermoacoustic instability is suppressed.

Mechanism behind suppression. – During the stable state of combustor operation, acoustic power production happens in small fragmented clusters. In contrast,

the acoustic power production occurs in large clusters during thermoacoustic instability [38]. Hence, we can deduce that by tracking the spatiotemporal dynamics of acoustic power sources during micro-jet injection, we would be able to unmask the mechanism behind suppression of thermoacoustic instability. To that end, we perform simultaneous acoustic pressure (p') measurement and high-speed chemiluminescence (CH^*) imaging of the flame during the micro-jet injections from the two pairs of ports in the top and bottom walls of the combustor in region A. The CH^* chemiluminescence represents the local heat release rate ($\dot{q}(x,y,t)$) as the intensity of the light emitted by CH^* radical is proportional to the chemical reaction rate [29]. Next, we consider a region of interest (length 20 mm and width 22 mm) at a distance of 5 mm downstream of the backward facing step (refer to fig. 1(b) in appendix A of the SM). The variation of p' is negligible across the region of interest at a given instant of time as the length of the combustion zone is very much smaller than the wavelength of the acoustic oscillations [39]. Hence, we consider the value of p' to be a constant in the region of interest at a given instant of time. We then multiply $p'(t)$ with the local heat release rate fluctuation ($\dot{q}'(x,y,t) = \dot{q}(x,y,t) - \bar{\dot{q}}(x,y)$) to obtain the spatial distribution of the local acoustic power ($p'\dot{q}'$) at a given instant of time [40].

To examine the spatiotemporal evolution of acoustic power sources ($p'\dot{q}' > 0$), we construct 2000 time-varying local acoustic power networks at each value of $(v_j/v_a)^2$. We consider every pixel of the $p'\dot{q}'$ image to be a node of the network. Since the computation of the network measures with the full resolution of the region of interest (202×184 pixels) is computationally very costly, we down-sampled the chemiluminescence images to 50% of the original resolution using bi-cubic interpolation [41]. With this downsampling, the number of nodes in the network is reduced from 37168 to 9292. Two nodes (i and j) are connected if and only if $(p'\dot{q}')_i$ and $(p'\dot{q}')_j \geq \epsilon$ and the Euclidean distance between the two given nodes is less than or equal to $\sqrt{2}$. Thus, we consider only the nearest neighbours when establishing a link, which enables us to track the spatiotemporal evolution of islands of acoustic power sources. We used ϵ (= 1.0; this value is 1.23% of the maximum local acoustic power production during thermoacoustic instability) to prevent the electronic noise in the high-speed camera, used for chemiluminescence measurements, from affecting the network computation.

Next, we compute the size of the largest cluster (S) of the local acoustic power network, at every instant of time. In graph theory, a connected component, or a cluster, of an undirected graph refers to a sub-graph in which any two nodes are connected to each other by a path, *i.e.*, a sequence of links [11]. The size of the giant cluster (S) refers to the number of nodes in the largest connected component of a network. In the present study, the connected component refers to the islands or clusters of acoustic power sources. To quantify the spatiotemporal evolution of islands of acoustic power sources, we compute S of the local acoustic power network for each of the 2000 networks for a given value of $(v_j/v_a)^2$. Figure 5 shows the variation of the average size of the largest cluster ($\bar{S}$) with respect to $(v_j/v_a)^2$. We observe that as we increase $(v_j/v_a)^2$, $\bar{S}$ also decreases along with p'_{rms}. In the absence of micro-jet injection, the variation in $\bar{S}$ is 1.73% when ϵ is increased from 0.8 to 1.2. Further, the variation in $\bar{S}$ is around 9.66% when the average is computed over 500 networks instead of 2000 networks. Now, let us examine how this suppression of p'_{rms} happens with micro-jet injection.

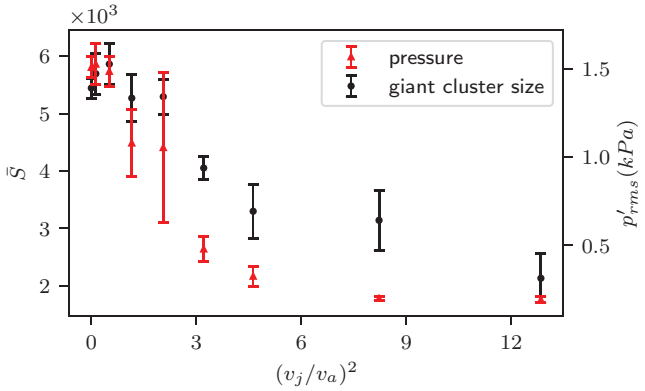

Fig. 5: The variation of $\bar{S}$ along with p'_{rms} with respect to $(v_j/v_a)^2$. Suppression of thermoacoustic instability occurs when large clusters of acoustic power sources disintegrates into small fragments. The error bars represent the standard deviation.

Recently, we investigated the emergence of large clusters of spatially coherent acoustic power sources at the onset of thermoacoustic instability from a state of spatially incoherent acoustic power production observed during the state of stable operation using complex networks [42]. We had constructed time-varying local acoustic power networks, as described in the present study, to track the spatiotemporal evolution of clusters of acoustic power sources during the transition to thermoacoustic instability. We found that the emergence of large clusters of spatially coherent acoustic power sources happens via nucleation, coalescence and growth of acoustic power sources as the acoustic pressure oscillations grow during intermittency. During the transition to thermoacoustic instability, we had shown that $\bar{S}$ gradually increases, indicating a percolation-like phase transition.

However, in the present study, $\bar{S}$ decreases with micro-jet injection (fig. 5). This resembles the phenomenon of inverse percolation as the combustor transitions from thermoacoustic instability to the state of stable operation with micro-jet injection [10]. At the optimum momentum flux ratio, the micro-jets disrupt the periodic coherent motion of the flow field observed during thermoacoustic instability, at the combustor inlet, above the bluff body shaft. This prevents the roll-up of the shear layer into large-scale vortices, which, in turn, averts the formation of large clusters of acoustic power sources. As the coherent

production of acoustic power ceases, the damping in the system overcomes the acoustic driving, leading to suppression of thermoacoustic oscillations. Hence, we can say that the suppression of large-amplitude thermoacoustic oscillation happens when the coherent production of acoustic power sources over large clusters ceases with an optimum momentum flux ratio of micro-jet injection at an optimal location.

The methodology presented here can be implemented in the design stage or the testing stage of gas turbine engines. Engineers obtain the velocity field from the computational fluid dynamic (CFD) simulations, such as the Large Eddy Simulations (LES), of the turbulent reactive flow [43]. They can then perform a correlation network analysis on the velocity field obtained during thermoacoustic instability and identify the critical region. Once the critical region is identified, they can effect changes in the design of the engine. Even in the testing stage, the analysis can be used to optimally redistribute the cooling air to target the critical region and disrupt the coherent power production.

Conclusions. – In summary, we have presented a novel approach to mitigate oscillatory instability in turbulent flows using complex networks. Traditionally, the optimal location for any passive control strategy is determined by a large number of trials; investing a humongous amount of money and time. The present approach using complex network analysis provides a simple, smart and efficient way to mitigate oscillatory instabilities by identifying the optimal location for implementing a passive control strategy. To the best of our knowledge, this is the first experimental evidence of suppression of oscillatory instability in a turbulent flow using a passive control strategy involving complex networks. The present approach can be extended to the control of other oscillatory instabilities in turbulent flows such as aeroacoustic [44] and aeroelastic instabilities [45]. We hypothesize that this novel approach can be used to implement flow control in separated and wall-bounded turbulent flows as well [46]. Also, we suggest that the identification of the critical region will help us to optimally locate the actuators, thus improving the efficiency of active control strategies. An improvement in the present methodology may be to use nonlinear measures such as mutual information [16], transfer entropy [47] or event synchronization [18] instead of Pearson's correlation, which is a linear measure, to construct spatial networks. This may lead to a better identification of critical regions to implement control strategies.

* * *

The authors wish to thank Mr. S. Thilagaraj and S. Anand for the support in performing the experiments. We thank Dr. T. Komarek and Prof. W. Polifke, Technical University of Munich, Germany, for the design of the combustor.

REFERENCES

[1] Lieuwen T. C. and Yang V., *Combustion Instabilities in Gas Turbine Engines: Operational Experience, Fundamental Mechanisms, and Modeling* (American Institute of Aeronautics and Astronautics) 2005.
[2] Rayleigh L., *Nature*, **18** (1878) 319.
[3] Juniper M. P. and Sujith R., *Annu. Rev. Fluid Mech.*, **50** (2018) 661.
[4] McManus K., Poinsot T. and Candel S. M., *Prog. Energy Combust. Sci.*, **19** (1993) 1.
[5] Schadow K. and Gutmark E., *Prog. Energy Combust. Sci.*, **18** (1992) 117.
[6] Oefelein J. C. and Yang V., *J. Propuls. Power*, **9** (1993) 657.
[7] Barabási A.-L., *Nat. Phys.*, **8** (2011) 14.
[8] Strogatz S. H., *Nature*, **410** (2001) 268.
[9] Boccaletti S., Latora V., Moreno Y., Chavez M. and Hwang D.-U., *Phys. Rep.*, **424** (2006) 175.
[10] Barabási A.-L., *Network Science* (Cambridge University Press) 2016.
[11] Newman M., *Networks: An Introduction* (Oxford University Press) 2010.
[12] Barthélemy M., *Phys. Rep.*, **499** (2011) 1.
[13] Finn E. S., Shen X., Scheinost D., Rosenberg M. D., Huang J., Chun M. M., Papademetris X. and Constable R. T., *Nat. Neurosci.*, **18** (2015) 1664.
[14] Eguiluz V. M., Chialvo D. R., Cecchi G. A., Baliki M. and Apkarian A. V., *Phys. Rev. Lett.*, **94** (2005) 018102.
[15] Zhou C., Zemanová L., Zamora G., Hilgetag C. C. and Kurths J., *Phys. Rev. Lett.*, **97** (2006) 238103.
[16] Donges J. F., Zou Y., Marwan N. and Kurths J., *Eur. Phys. J. ST*, **174** (2009) 157.
[17] Tsonis A. A. and Roebber P. J., *Phys. A: Stat. Mech. Appl.*, **333** (2004) 497.
[18] Malik N., Bookhagen B., Marwan N. and Kurths J., *Clim. Dyn.*, **39** (2012) 971.
[19] Boers N., Goswami B., Rheinwalt A., Bookhagen B., Hoskins B. and Kurths J., *Nature*, **566** (2019) 373.
[20] Gao Z. and Jin N., *Phys. Rev. E*, **79** (2009) 066303.
[21] Molkenthin N., Rehfeld K., Marwan N. and Kurths J., *Sci. Rep.*, **4** (2014) 4119.
[22] Tupikina L., Molkenthin N., López C., Hernández-García E., Marwan N. and Kurths J., *PLoS ONE*, **11** (2016) e0153703.
[23] Russo L., Russo P. and Siettos C. I., *PLoS ONE*, **11** (2016) e0163226.
[24] Tang J., Mascolo C., Musolesi M. and Latora V., *Exploiting temporal complex network metrics in mobile malware containment*, in *Proceedings of 2011 IEEE International Symposium on a World of Wireless, Mobile and Multimedia Networks* (IEEE) 2011, pp. 1–9.
[25] Taira K., Nair A. G. and Brunton S. L., *J. Fluid Mech.*, **795** (2016) R2.
[26] Unni V. R., Krishnan A., Manikandan R., George N. B., Sujith R., Marwan N. and Kurths J., *Chaos*, **28** (2018) 063125.
[27] Unni V. R., Nair S. R. I., Krishnan A., Marwan N. and Kurths J., *System and method for optimizing passive*

control of oscillatory instabilities in turbulent flows, US Patent App. 16/287, 248 (August 29 2019).

[28] Raffel M., Willert C. E., Scarano F., Kähler C. J., Wereley S. T. and Kompenhans J., *Particle Image Velocimetry: A Practical Guide* (Springer) 2018.

[29] Hardalupas Y. and Orain M., *Combust. Flame*, **139** (2004) 188.

[30] Horvath S., *Weighted Network Analysis: Applications in Genomics and Systems Biology* (Springer Science & Business Media) 2011.

[31] Zhang B. and Horvath S., *Stat. Appl. Genet. Mol. Biol.*, **4** (2005) 1–43.

[32] Mumford J. A., Horvath S., Oldham M. C., Langfelder P., Geschwind D. H. and Poldrack R. A., *Neuroimage*, **52** (2010) 1465.

[33] Onnela J.-P., Saramäki J., Kertész J. and Kaski K., *Phys. Rev. E*, **71** (2005) 065103.

[34] Kim H.-J., Lee Y., Kahng B. and Kim I.-m., *J. Phys. Soc. Jpn.*, **71** (2002) 2133.

[35] Holme P., Park S. M., Kim B. J. and Edling C. R., *Phys. A: Stat. Mech. Appl.*, **373** (2007) 821.

[36] Opsahl T., Agneessens F. and Skvoretz J., *Soc. Netw.*, **32** (2010) 245.

[37] George N. B., Unni V. R., Raghunathan M. and Sujith R., *J. Fluid Mech.*, **849** (2018) 615.

[38] Mondal S., Unni V. R. and Sujith R., *J. Fluid Mech.*, **811** (2017) 659.

[39] Nair V., Thampi G. and Sujith R., *J. Fluid Mech.*, **756** (2014) 470.

[40] Poinsot T. and Veynante D., *Theoretical and Numerical Combustion* (RT Edwards, Inc.) 2005.

[41] Zhang Y., Zhao D., Zhang J., Xiong R. and Gao W., *IEEE Trans. Image Process.*, **20** (2011) 3291.

[42] Krishnan A., Sujith R., Marwan N. and Kurths J., *J. Fluid Mech.*, **874** (2019) 455.

[43] Menon Suresh and Jou Wen-Huei, *Combust. Sci. Technol.*, **75** (1991) 53.

[44] Heller H. H., Holmes D. and Covert E. E., *J. Sound Vib.*, **18** (1971) 545.

[45] Vaurigaud B., Manevitch L. I. and Lamarque C.-H., *J. Sound Vib.*, **330** (2011) 2580.

[46] Fiedler H. and Fernholz H.-H., *Prog. Aerospace Sci.*, **27** (1990) 305.

[47] Wibral M., Rahm B., Rieder M., Lindner M., Vicente R. and Kaiser J., *Prog. Biophys. Mol. Biol.*, **105** (2011) 80.